Journal of Molecular Structure 1044 (2013) 248–254

Contents lists available at SciVerse ScienceDirect

Journal of Molecular Structure

journal homepage: www.elsevier.com/locate/molstruc

Microstructural characterizations of different Mn-oxide nanoparticles used as models in toxicity studies

Marijan Gotić [a,*], Tanja Jurkin [a,*], Svetozar Musić [a,*], Klaus Unfried [b], Ulrich Sydlik [b], Anamarija Bauer-Šegvić [c]

[a] Division of Materials Chemistry, Ruđer Bošković Institute, HR-10002 Zagreb, Croatia
[b] Toxicology Group, Institut für Umweltmedizinische Forschung, Düsseldorf, Germany
[c] Clinical Hospital Dubrava, Department of Pathology, 10000 Zagreb, Croatia

HIGHLIGHTS

- The synthesis and properties of Mn_3O_4, γ-MnOOH and MnO_2 nanoparticles of various morphologies were investigated.
- Influence of divalent metal cations on the crystal structure and morphology of MnO_2 nanoparticles was shown.
- Possible use of Mn-oxide nanoparticles in toxicity studies is shown.

ARTICLE INFO

Article history:
Available online 8 October 2012

Keywords:
Mn-oxides
Manganese oxides
Nanoparticles
Microstructures
Toxicity

ABSTRACT

Mn-oxide microstructures were investigated by XRD, FT-IR, TEM, FE SEM and EDS techniques. The oxidation of the aqueous solutions of manganese (II) chloride by hydrogen peroxide was employed to synthesize pure 20–30-nm pseudospherical hausmannite (Mn_3O_4) nanoparticles and manganite (γ-MnOOH) nanowires. The α-MnO_2 nanotubes and nanorods were hydrothermally synthesized starting from a $KMnO_4$ precursor, then modified with the addition of divalent metal cations Mn^{2+}, Cu^{2+}, Ni^{2+} and Fe^{2+}. The modification with Mn^{2+} induced the transformation of α-MnO_2 nanotube into 3D β-MnO_2 (pyrolusite) prismatic nanoparticles, whereas the low-crystalline α-MnO_2 nanorods were transformed into disk-like γ-MnO_2 nanoparticles. The modification with Cu^{2+} and Ni^{2+} induced the structural transformation of α-MnO_2 into a mixture of MnO_2 polymorphs. The modification with Cu^{2+} decreased, whereas the modification with Ni^{2+} improved the crystallinity of MnO_2. The modification with Fe^{2+} induced the structural transformation of α-MnO_2 into γ-MnO_2, a decrease in crystallinity and the segregation of α-Fe_2O_3 (hematite). Thus the modification of MnO_2 with Fe^{2+} (Mn^{2+}) divalent metal cations that can be oxidized into Fe^{3+} (Mn^{4+}) by a $KMnO_4$ precursor differs significantly in comparison with, in this case, non-oxidizable cations such as Cu^{2+} and Ni^{2+}. On the other hand, the advantage that the modification of MnO_2 with Mn^{2+} produces chemically identical compounds with different morphology can be used as a model system for toxicity studies. In this work the preliminary measurements of intracellular oxidative stress in epithelial cells induced by manganese oxide nanoparticles are reported.

1. Introduction

Manganese oxides have found application in catalysis, ion-exchange reactions, as cathode materials for rechargeable batteries and as contrast agents for magnetic resonance imaging (MRI). The manganese oxide nanoparticles have been used to improve the mechanical and thermal properties of polymers [1] and to enhance the ionic conductivity of polymer electrolytes [2]. On the other hand, manganese ore processing, metallurgy and metalworking are potential sources of inhalational exposure to manganese oxide particles [3]. Manganese oxides occur in a variety of oxidation states and chemical and structural forms. Due to their unique properties and wide applications, the synthesis of manganese oxide nanoparticles has been investigated in order to put their chemical composition, structure [4], size and morphology [5–11] under control.

In a previous work [12] the morphologies of α-Fe_2O_3 particles were modified by adding divalent metal cations. They gradually modified the α-Fe_2O_3 spindles to a pseudosphere and the nanotube to nanoring particle morphologies. A modification with the divalent

* Corresponding authors. Tel.: +385 1 4561 111.
E-mail addresses: gotic@irb.hr (M. Gotić), tjurkin@irb.hr (T. Jurkin), music@irb.hr (S. Musić).

0022-2860/$ - see front matter © 2012 Elsevier B.V. All rights reserved.
http://dx.doi.org/10.1016/j.molstruc.2012.09.083

metal cations (Mn^{2+}, Cu^{2+}, Zn^{2+} and Ni^{2+}) induced changes in the morphology of α-Fe_2O_3 particles, but had no impact on the chemical composition of α-Fe_2O_3 particles. This is because upon exposure to hydrothermal and acidic conditions ($pH \leqslant 2$) the divalent metal cations do not precipitate or adsorb on the α-Fe_2O_3 particles [12]. Taking into account the results obtained with α-Fe_2O_3, it was interesting to compare these results with those obtained during the precipitation of MnO_2 in the presence of certain divalent cations. The modification of 1D MnO_2 structures with the divalent metal cations showed quite different behavior in comparison with the α-Fe_2O_3 modifications. This is because of the $KMnO_4$ precursor that can be readily involved in the oxidation/reduction reactions. Furthermore, manganese dioxide appears in a number of different polymorphic forms, such as α-MnO_2, β-MnO_2, γ-MnO_2, ε-MnO_2, λ-MnO_2 and δ-MnO_2. In all MnO_2 polymorphs the main structural framework comprises edge- or corner-sharing MnO_6 octahedra, but the way in which the basic octahedral MnO_6 units are linked together is different [13]. Different rearrangements of MnO_6 octahedra give rise to manganese oxides with tunnel and layered structures, which exhibit cation-exchange and molecule adsorptive properties, like zeolites and clay minerals [14].

In the present study we describe the synthesis and microstructural properties of pseudospherical hausmannite (Mn_3O_4) and 1D manganite (γ-MnOOH) nanoparticles. MnO_2 particles in the form of nanorods or nanotubes (1D morphologies) were synthesized by applying hydrothermal approach [12]. The 1D morphologies of MnO_2 particles were then modified by the addition of Mn^{2+}, Cu^{2+}, Fe^{2+} and Ni^{2+} cations. The influence of divalent metal cations on the MnO_2 structure and nanoparticle morphology was studied. The synthesized manganese oxide nanoparticles were used as a model system for the toxicity study. In this work the preliminary measurements of intracellular oxidative stress in epithelial cells induced by synthesized manganese oxides nanoparticles are shown.

2. Experimental

2.1. Chemicals

The chemicals $KMnO_4$, $MnCl_2{\cdot}4H_2O$, $CuCl_2{\cdot}2H_2O$, $NiCl_2{\cdot}6H_2O$, $FeCl_2$ anhydrous, $FeCl_3{\cdot}6H_2O$, concentrated H_2O_2 (30%), HCl (37%) and NH_3 aq. (25%) solutions of analytical grade purity were supplied by *Kemika*, Zagreb. Twice-distilled water was also used. Stock solution of $FeCl_2$ was prepared by dissolving 0.1 mol of $FeCl_2$ in 50 ml of 2 M HCl.

2.2. Sample preparation

The preparation of Mn_3O_4 (hausmannite) was based on the oxidation of an $MnCl_2$ solution with a concentrated H_2O_2 solution, followed by the addition of an NH_3 aq. solution. The suspension thus obtained was treated at 90 °C. The same procedure was applied in the preparation of γ-MnOOH (manganite), except that the NH_3 aq. solution was added to the $MnCl_2$ solution prior to the addition of the H_2O_2. Details of these procedures are described elsewhere [15].

MnO_2 was prepared by applying hydrothermal approach. In a typical experimental procedure 2.6 mmol of $KMnO_4$ was added to an acidic aqueous solution (1.1 mmol of conc. HCl + 45 ml of doubly-distilled water) and transferred into a 50 ml Teflon-lined stainless steel autoclave. The autoclave was sealed, put into a cold oven and heated at 140 °C for 3 or 14 h. The autoclave was cooled down to room temperature, the precipitate was separated by centrifugation, rinsed with double distilled water several times and dried overnight at 60 °C. Modification with the divalent cations was performed by the substitution of a certain amount of Mn^{2+}, Ni^{2+}, Cu^{2+}, Fe^{2+} and Fe^{3+} cations for the Mn^{7+} precursor. For example, for 70 mol% of Mn^{2+} in solution ($[Mn^{2+}]/([Mn^{7+}] + [Mn^{2+}]) = 0.7$), 1.82 of $MnCl_2$ + 0.78 mmol of $KMnO_4$ was added to 45 ml of doubly-distilled water, stirred for 1 h and followed by the same experimental procedure described for a pure $KMnO_4$ sample. The samples modified with Mn^{2+} and autoclaved at 140 °C for 3 h are marked from S0 to S7. The samples modified with Mn^{2+} and autoclaved for 14 h are marked from S8 to S11, whereas

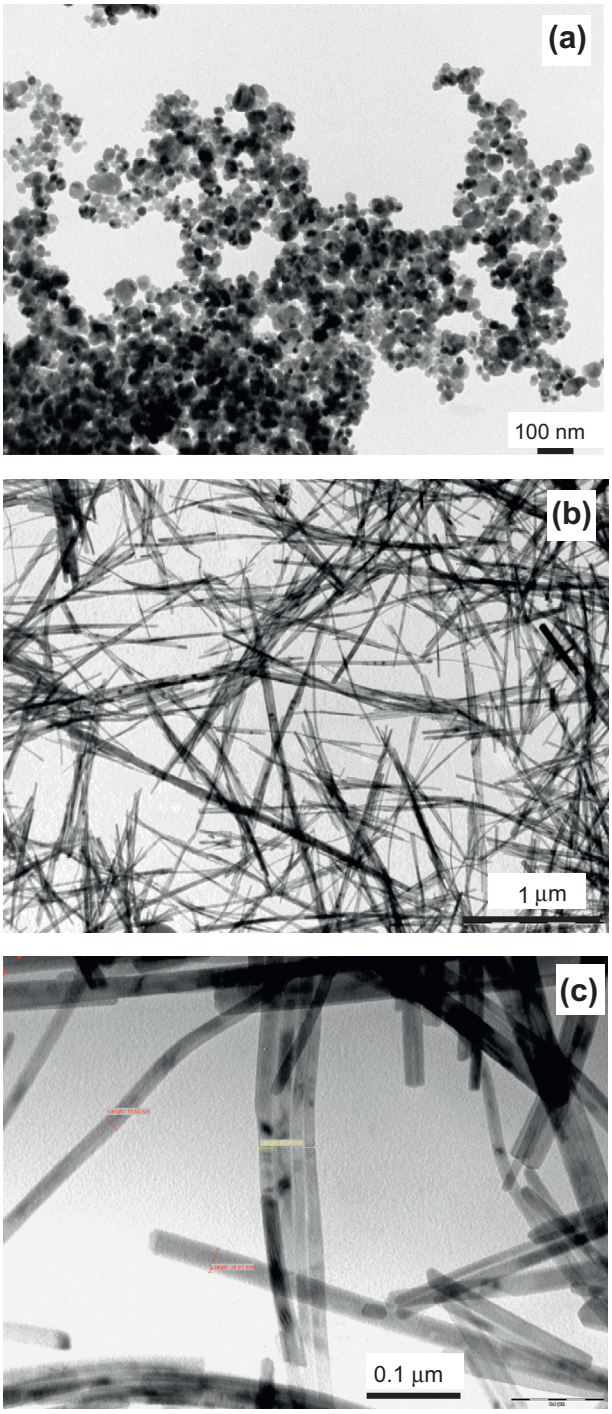

Fig. 1. (a) TEM images of the synthesized Mn_3O_4 (hausmannite) pseudospherical nanoparticles, with majority of nanoparticles at 20–30 nm; (b) TEM images of the synthesized γ-MnOOH (manganite) nanoparticles showing 1D nanoparticles of about 1–2 μm in length; and (c) TEM images of γ-MnOOH nanoparticles at high magnification showing lateral arraying. The estimated width of these 1D nanoparticles is about 20 nm.

the samples autoclaved for 14 h and modified with Cu^{2+}, Ni^{2+}, Fe^{2+} and Fe^{3+} are marked from S12 to S15. Detailed experimental conditions for the synthesis of MnO_2 nanoparticles are given in Table S1 (Supporting information).

2.3. Reactive oxygen species (ROS) detection

The generation of ROS was determined intracellularly using the fluorogenic probe H_2DCF-DA (2′,7′-dichlorofluorescein diacetate) from *Calbiochem* (Schwalbach, Germany). H_2DCF-DA is lipid-soluble and nonfluorescent. Cleavage of the diacetate group, either enzymatically by intracellular esterases or chemically by alkaline hydrolysis, yields the lipid insoluble, nonfluorescent probe DCFH. Oxidation of DCFH by ROS results in a highly fluorescent probe 2′,7′-dichlorofluorescein (DCF), which can be detected and quantified fluorometrically.

2.4. Sample characterization

The synthesized samples were analyzed using powder X-ray diffraction (XRD), Fourier Transform-Infrared (FT-IR) and Mössbauer spectroscopy, Transsmision Electron Microscopy (TEM) and Field Emission Scanning Electron Microscope-Energy Dispersive Spectroscopy (FE SEM-EDS).

XRD patterns were recorded at 20 °C with an APD 2000 X-ray powder diffractometer using CuKα (λ = 1.54059 Å) radiation (40 kV and 30 mA conditions), graphite monochromator, NaI-Tl detector manufactured by *ItalStructures*, Riva del Garda, Italy. The XRD patterns were recorded over a 12–80° 2θ range with 2θ step of 0.03° and a counting time per step of 11–29 s. The samples were recorded using an aluminium or XRD zero-quartz holder.

The *Jeol Ltd.* thermal field emission scanning electron microscope (FE-SEM), model JSM-7000F was connected to the Oxford EDS/INCA 350 (energy dispersive X-ray spectrometer). The TEM produced by *Jeol Ltd.* was also used.

^{57}Fe Mössbauer spectra were recorded in the transmission mode using a standard instrumental configuration by *WissEl GmbH* (Starnberg, Germany). The ^{57}Co in the rhodium matrix was used as a Mössbauer source. The spectrometer was calibrated at 20 °C using the standard α-Fe foil spectrum. The velocity scale and all the data refer to the metallic α-Fe absorber at 20 °C. The experimentally observed Mössbauer spectra were fitted using the *MossWinn* program.

The Fourier transform infrared (FT-IR) spectra were recorded at 20 °C using a *Perkin–Elmer* spectrometer model 2000. The specimens were pressed into small disks using a spectroscopically pure KBr matrix. The spectra were recorded using a KBr beam splitter in the mid IR region (4000–400 cm^{-1}).

3. Results and discussion

Fig. 1 shows the TEM images of synthesized Mn_3O_4 (a) and γ-MnOOH (b and c) nanoparticles. The synthesized Mn_3O_4 nanoparticles are of pseudospherical shape with most of them being 20–30 nm in size. The structural characterization of this sample can be found in our previous work [16]. The synthesized γ-MnOOH nanoparticles (b) show 1D morphology with lengths in micrometer range, whereas the widths of these nanowires are about 20 nm.

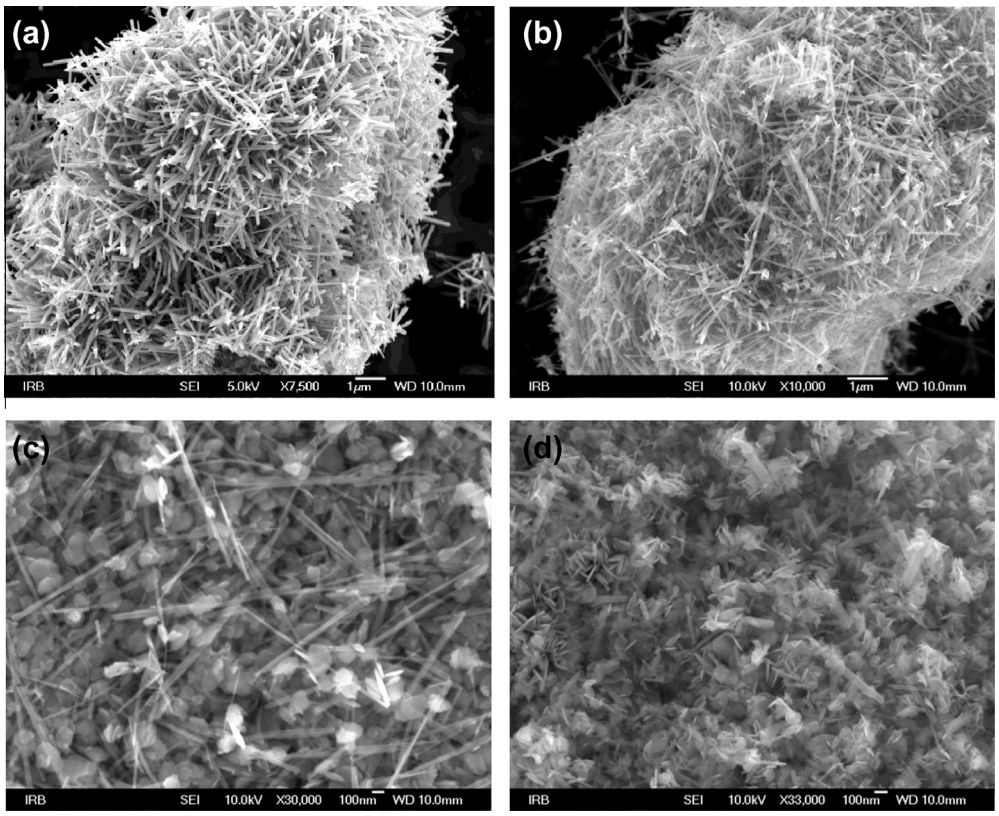

Fig. 2. FE SEM images of the synthesized MnO_2 samples S0, S3, S5 and S7. The samples were autoclaved for 3 h, the precursor was $KMnO_4$, and modification was performed with $MnCl_2$. Fig. 2a shows an unmodified sample S0 that consists of nanorods having 1.2–1.6 μm in length and the estimated width about 70 nm. Fig. 2b shows sample S3 modified with 30 mol% of Mn^{2+}. Sample S3 consists of two kinds of nanoparticles: nanorods of 1.5–2.0 μm in length and small 3D irregular nanoparticles of about 100 nm in size. Fig. 3c shows sample S5 modified with 50 mol% of Mn^{2+}. Sample S5 consists of 3D irregular nanoparticles and nanorods. The size of irregular nanoparticles is about 150–200 nm, whereas the length of nanorods is about 0.7–1.0 μm. Fig. 2d shows sample S7 modified with 70 mol% of Mn^{2+}. Sample S7 consists mostly of 2D and 3D irregular nanoparticles, whereas wide irregular nanorods are also present.

The TEM image of γ-MnOOH nanoparticles at high magnification (c) shows a tendency of lateral arraying. The XRD patterns and FT-IR spectra of these nanoparticles are shown in Figs. S1 and S2 (Supporting information).

Fig. 2 shows the FE SEM images of synthesized MnO_2 nanoparticles. The starting morphologies are nanorods of 1.2–1.6 μm in length (a) that were synthesized hydrothermally from the $KMnO_4$ precursor upon autoclaving at 140 °C for 3 h. The starting morphology was then modified with Mn^{2+} metal cations. The modification with 30 mol% of Mn^{2+}, (b) produced two kinds of nanoparticles; nanorods of 1.5–2.0 μm in length and small 3D irregular nanoparticles sized about 100 nm. The modification with 50 mol% of Mn^{2+}, (c) yielded 3D irregular nanoparticles and nanorods, whereas the modification with 70 mol% of Mn^{2+} and (d) yielded disk-like nanoparticles (2D morphology) and irregular nanorods.

The corresponding XRD patterns of the synthesized samples (Fig. 3) showed that sample S1 (10 mol% Mn^{2+}) consists of a pure α-MnO_2 phase, sample S7 (70 mol% Mn^{2+}) of a pure γ-MnO_2 phase, whereas the samples modified with 40 and 60 mol% of Mn^{2+} (S4 and S6) are mixtures of the two phases.

Fig. 4 shows the FT-IR spectra of samples S0 to S7. The samples were autoclaved for 3 h, the precursor was $KMnO_4$. Sample S0 was unmodified, whereas samples S1, S3, S5, S6 and S7 were modified with 10, 30, 50, 60 and 70 mol% of Mn^{2+}, respectively. The FT-IR spectra results in the region of 800–400 cm^{-1} provide information about the MnO_6 octahedra. The difference in vibrational bands is linked to the MnO_6 polymerization, i.e., the variation in the edge-sharing of octahedra [17,18]. Samples S0 and S1 are characterized by four FT-IR bands at 718, 595, 535 and 476 cm^{-1} that can be assigned to α-MnO_2, since the XRD patterns of these two samples corresponded to a pure α-MnO_2 phase. The α-MnO_2 possesses the hollandite-type (2 × 2 tunnels) structure which consists of MnO_6 octahedra sharing edges to form double chains. The dominant absorption band at 535 cm^{-1} is due to the displacement of oxygen anions relative to manganese cations along the direction of the octahedral chains, whereas the stretching mode of MnO_6 octahedra along the double chain is located at 718 cm^{-1} [17,18]. When modified with Mn^{2+}, the α-MnO_2 transforms into γ-MnO_2, and as a consequence the dominant FT-IR band at 535 cm^{-1} splits into two bands and at the end turns into a broad band at about 545 cm^{-1}.

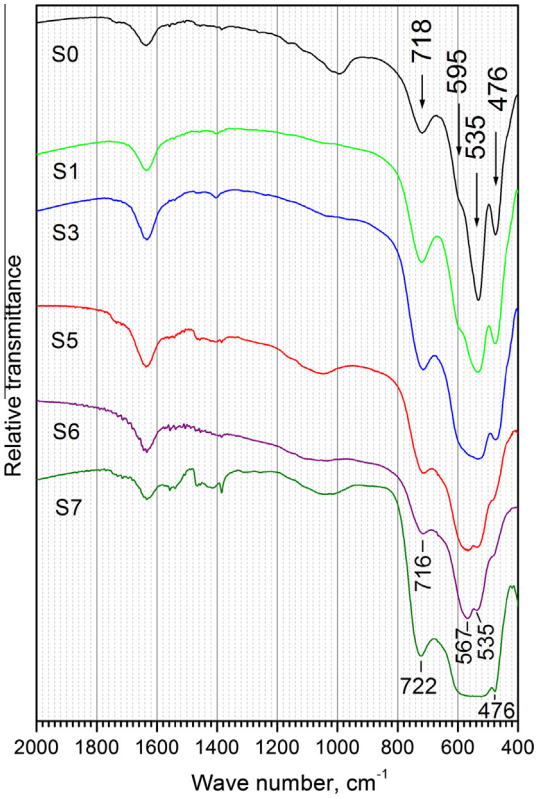

Fig. 4. The FT-IR spectra of samples S0, S1, S3, S5, S6 and S7. The samples were autoclaved for 3 h, the precursor was $KMnO_4$, and modification was performed with $MnCl_2$. Sample S0 is unmodified, whereas samples S1, S3, S5, S6 and S7 were modified with 10, 30, 50, 60 and 70 mol% of Mn^{2+}, respectively.

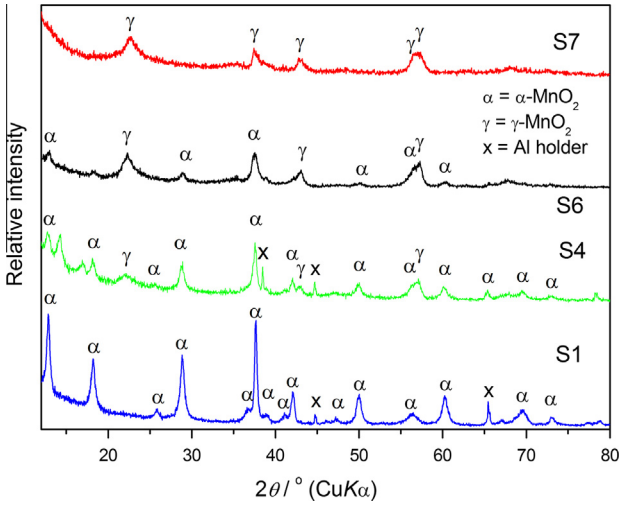

Fig. 3. XRD patterns of synthesized samples S1, S4, S6 and S7. The samples were autoclaved for 3 h, the precursor was $KMnO_4$, and modification was performed with $MnCl_2$. Sample S1 (10 mol% Mn^{2+}) consists of a pure α-MnO_2 phase (assigned in accordance with the ICDD PDF card No. 44-0141). Sample S7 (70 mol% Mn^{2+}) consists of a pure γ-MnO_2 phase (assigned in accordance with the ICDD PDF card No. 14-0644). Samples modified with 40 and 60 mol% of Mn^{2+} (S4 and S6) consist of both phases. The peaks denoted with **x** belong to an Al holder.

Fig. 5 shows the FE SEM images of the synthesized MnO_2 samples S8, S9 and S11. The precursor was $KMnO_4$ and the samples were autoclaved for 14 h. Under these conditions nanotubes were formed (a) in the length of about 1.2–2.0 μm and the width of about 80 nm. Upon modification with 20 mol% of Mn^{2+}, (b) the nanotubes transformed mostly to nanorods and irregular nanoparticles. When modified with 70 mol% Mn^{2+} and (c), the nanotubes transformed into 3D prismatic particles of varying size (0.5–1.5 mm).

Fig. 6 shows the XRD patterns of synthesized samples S8, S10 and S11. The unmodified sample S8 consists of a pure α-MnO_2 phase. Sample S10 (30 mol% Mn^{2+}) is a mixture of α-MnO_2, β-MnO_2 and γ-MnO_2 phases, whereas the sample S11 (70 mol% Mn^{2+}) consists of a virtually pure β-MnO_2 phase. Therefore, in a pure system when only the permanganate (MnO_4^-) ions were present, the precipitate consisted exclusively of α-MnO_2. With the addition of 30 mol% Mn^{2+}, a mixture of α-MnO_2 and β-MnO_2 was present, whereas at 70 mol% Mn^{2+} a pure β-MnO_2 (pyrolusite) was formed. The particle morphology changed from 1D to 3D with an increase in the Mn^{2+} concentration (Fig. 5). Likewise, the concentrations of K^+ ions decreased with an increase in the Mn^{2+} addition, as shown by EDS (Table S1). The presence of hydrated K^+ ions (137 pm) stabilized the 2 × 2 channel structure of α-MnO_2 and, as a result, in a pure system exclusively α-MnO_2 was formed. With an addition of $MnCl_2$ the relative concentration of K^+ decreased and consequently a β-MnO_2 polymorph was stabilised (by small H^+ ions). The change in the morphology suggests that β-MnO_2 particles were formed by the dissolution–recrystallization mechanism.

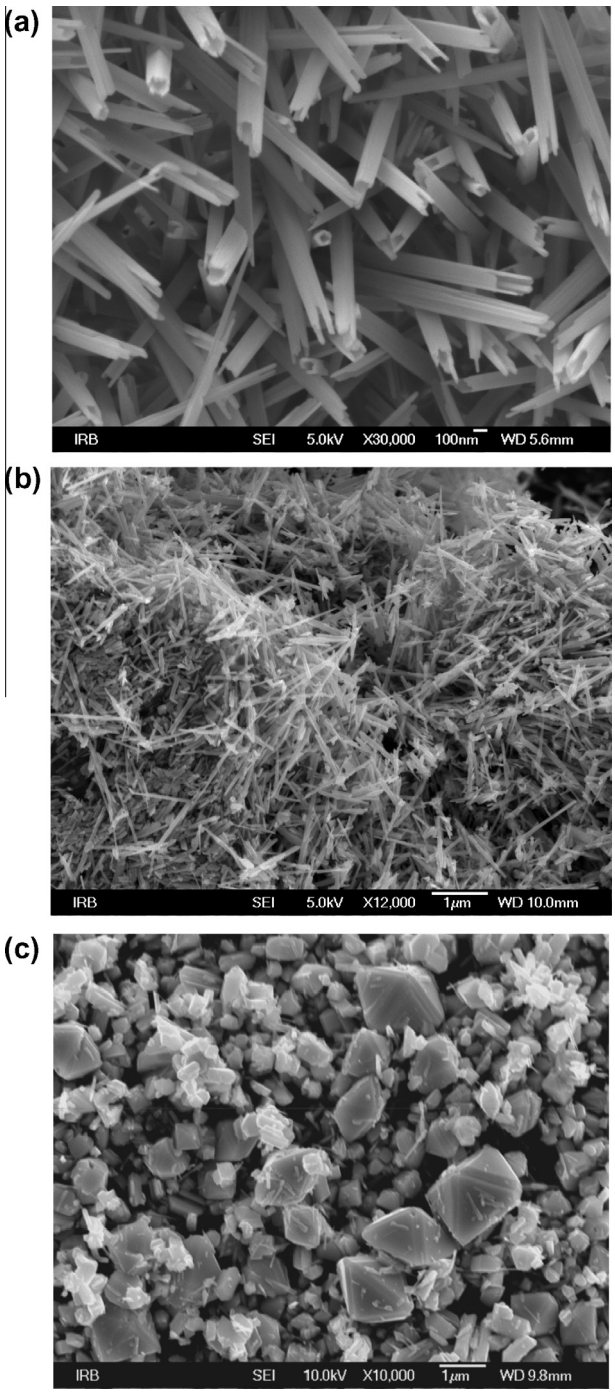

Fig. 5. The FE SEM images of the synthesized MnO_2 samples S8, S9 and S11. The samples were autoclaved for 14 h, the precursor was $KMnO_4$, and modification was performed with $MnCl_2$. Fig. 5a shows an unmodified sample S8 of nanotube morphology. The length of nanotubes is about 1.2–2.0 μm and the width about 80 nm. Fig. 5b shows sample S9 modified with 20 mol% Mn^{2+}. The modified sample S9 does not have tubular morphology, it consists mostly of nanorods and a small amount of irregular nanoparticles. Fig. 5c shows sample S11 modified with 70 mol% of Mn^{2+}. The sample consists of 3D prismatic particles of various sizes (0.5–1.5 mm).

Fig. 7 shows the FE SEM images of synthesized MnO_2 samples S12, S13 and S14. The sample modified with 70 mol% Cu^{2+} (a) consists of nanorods and irregular 3D nanoparticles. Fig. 7b shows sample S13 modified with 70 mol% Ni^{2+}. It consists of broad irregular nanorods and 3D irregular nanoparticles. Fig. 7c shows sample S14 modified with 70 mol% Fe^{2+}. This sample consists of large 3D

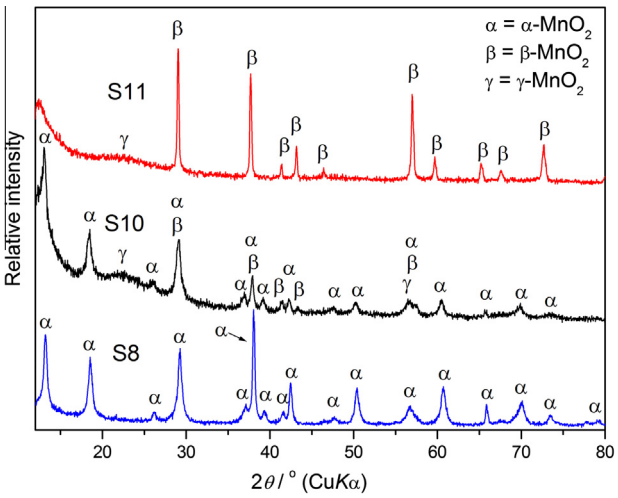

Fig. 6. The XRD patterns of synthesized samples S8, S10 and S11. The samples were autoclaved for 14 h, the precursor was $KMnO_4$, and modification was performed with $MnCl_2$. The unmodified sample S8 consists of a pure α-MnO_2 phase (assigned in accordance with the ICDD PDF card No. 44-0141). Sample S10 (30 mol% Mn^{2+}) is a mixture of α-MnO_2, β-MnO_2 and γ-MnO_2 phases, whereas sample S11 (70 mol% Mn^{2+}) consists of the virtually pure β-MnO_2 phase. γ-MnO_2 phase is assigned in accordance with the ICDD PDF card No. 14-0644. β-MnO_2 is assigned in accordance with the ICDD PDF card No. 24-0735.

irregular particles of about 1–3 μm in size. Much smaller nanoparticles adsorbed on the larger ones are also visible. The EDS analysis of sample S12, S13 and S14 are shown in Figs. S3, S4 and S5, respectively.

Fig. 8 shows the XRD patterns of samples S12, S13 and S14 modified with 70 mol% of Cu^{2+}, Ni^{2+} and Fe^{2+}, respectively. The modification with Cu^{2+} and Ni^{2+} induced the structural transformation of α-MnO_2 into a mixture of MnO_2 polymorphs. The modification with Cu^{2+} caused a decrease in MnO_2 crystallinity, whereas the segregation of CuO as a separate phase could not be proved. The modification with Ni^{2+} improved the crystallinity of MnO_2. The modification with Fe^{2+} induced the structural transformation of α-MnO_2 into γ-MnO_2, a decrease in crystallinity and the segregation of α-Fe_2O_3 (hematite). Thus the modification of MnO_2 with the Fe^{2+} divalent metal cations that can be oxidized into Fe^{3+} by the $KMnO_4$ precursor differs significantly in comparison with, in this case, the non-oxidizable cations such as Cu^{2+} and Ni^{2+}.

Fig. 9 shows the Mössbauer spectra of samples S14 and S15 modified with 70 mol% Fe^{2+} and 70 mol% Fe^{3+}, respectively. The modification with Fe^{3+} was performed with a view to comparing the behavior of Fe^{3+} versus Fe^{2+} modification. Basically, the both spectra show the presence of a sextet, the parameters of which belong to α-Fe_2O_3 (hematite), and a doublet that corresponds to paramagnetic or superparamagnetic particles. However, the amount of hematite is much higher in the case of Fe^{2+} modification. The Mössbauer results are in line with the SEM and EDS results for samples S14 and S15 (Figs. S5, S6 and S7).

The modification with Mn^{2+} or Fe^{2+} is different compared with the modification with Cu^{2+} and Ni^{2+}. This is because Mn^{2+} or Fe^{2+} can reduce Mn^{7+} to Mn^{4+}, whereas Cu^{2+} and Ni^{2+} cannot. Actually, in the investigated pure system (acidic aqueous solution of $KMnO_4 + HCl + H_2O$), the MnO_4^- solution is intrinsically unstable in an acid medium and slightly disproportionate to MnO_2 at room temperature [19]. In the presence of chloride (Cl^-) the permanganate (MnO_4^-) solution can be reduced to Mn^{4+} or even to Mn^{2+} (Eq. (1)), which, once formed, acts as a reducing agent for permanganate ions and again Mn^{4+} precipitated as MnO_2 (Eq. (2)). During the reduction of the permanganate (Mn^{7+}) ion oxygen can be oxidized to O_2 (Eq. (4)) as well as chloride (Cl^-) to chlorine (Cl_2) (Eq.

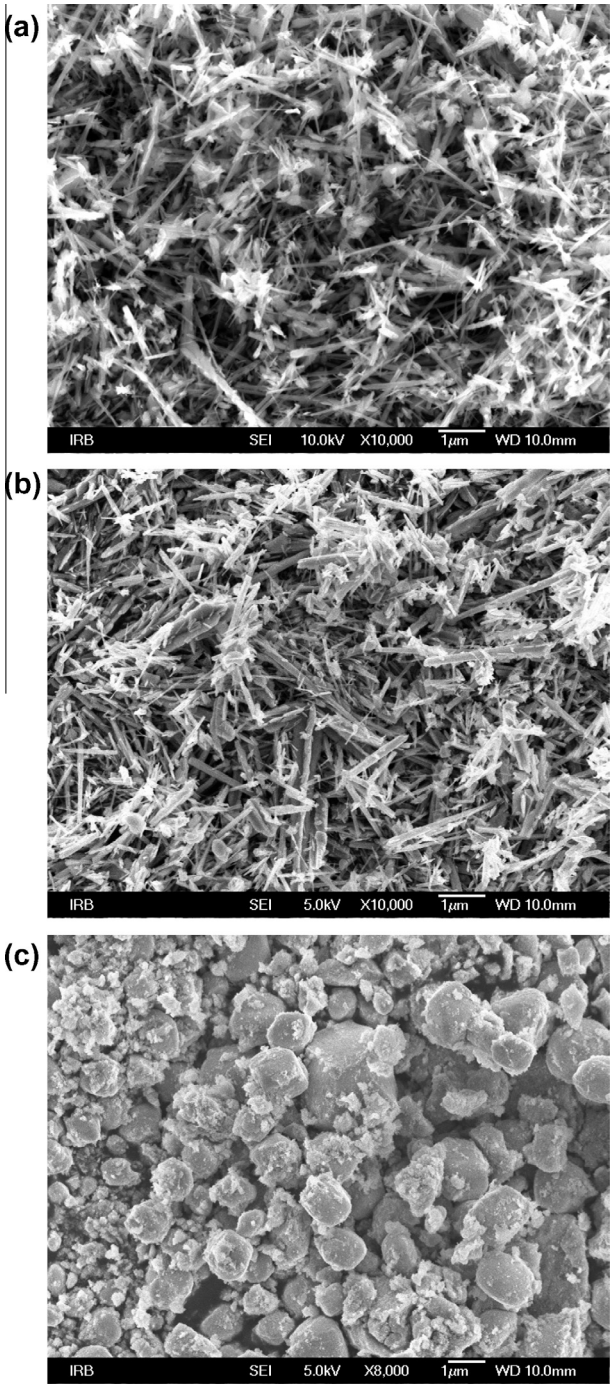

Fig. 7. The FE SEM images of synthesized MnO_2 samples S12, S13 and S14. The samples were autoclaved for 14 h, the precursor was $KMnO_4$ and modification was performed with $CuCl_2$, $NiCl_2$ and $FeCl_2$. Fig. 7a shows sample S12 modified with 70 mol% Cu^{2+}. This sample consists of nanorods and irregular 3D nanoparticles. Fig. 7b shows sample S13 modified with 70 mol% Ni^{2+}. It consists of broad irregular nanorods and 3D irregular nanoparticles. Fig. 7c shows sample S14 modified with 70 mol% Fe^{2+}. This sample consists of large 3D irregular particles of about 1–3 μm size. The much smaller nanoparticles adsorbed on the bigger one are also visible.

(1)). Also, the formed chlorine can oxidize Mn^{2+} to Mn^{4+} and MnO_2 precipitate (Eq. (3)) [20]. At the hydrothermal condition in the autoclave at 140 °C all reactions are accelerated and the yields are relatively high.

$$2MnO_4^- + 16H^+ + 10Cl^- \rightarrow 2Mn^{2+} + 8H_2O + 5Cl_2 \quad (1)$$

$$2MnO_4^- + 3Mn^{2+} + 2H_2O \rightarrow 5MnO_2 + 4H^+ \quad (2)$$

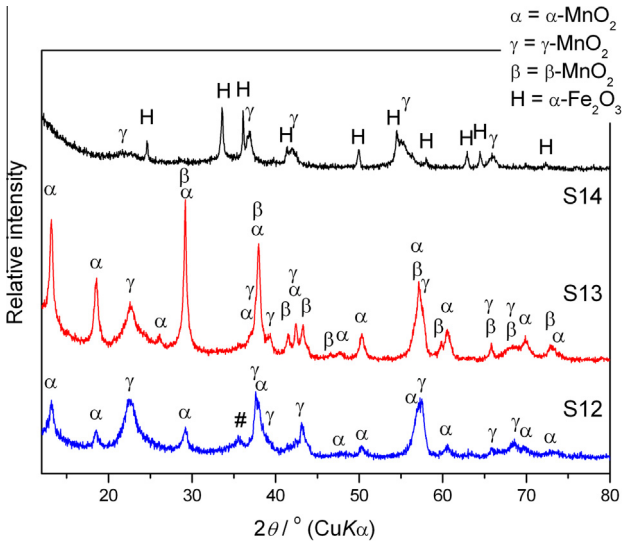

Fig. 8. The XRD patterns of synthesized MnO_2 samples S12, S13 and S14 modified with 70 mol% Cu^{2+}, Ni^{2+} and Fe^{2+}, respectively. α-MnO_2 is assigned in accordance with the ICDD PDF card No. 44-0141, γ-MnO_2 in accordance with the ICDD PDF card No. 14-0644, β-MnO_2 in accordance with the ICDD PDF card No. 24-0735 and α-Fe_2O_3 in accordance with the ICDD PDF card No. 33-0644. The diffraction line at 35.6 2θ/° (CuKα) denoted with # could not be assigned with certainty.

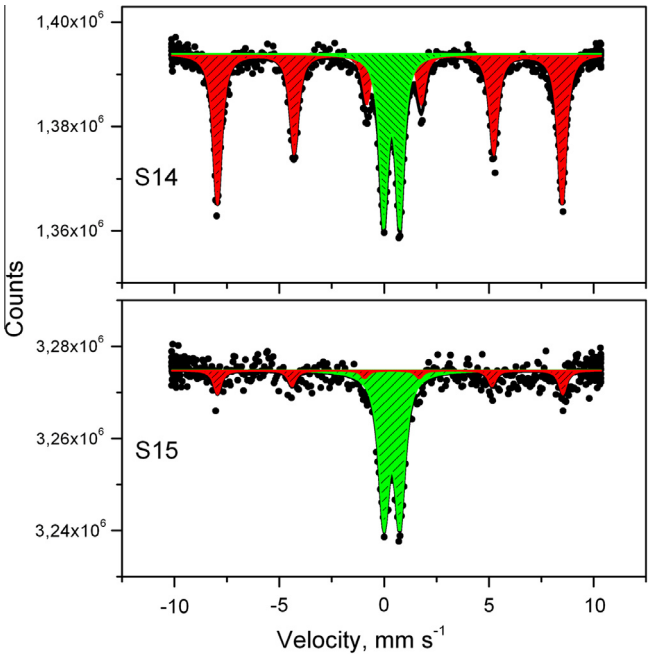

Fig. 9. The room temperature ^{57}Fe Mössbauer spectra of samples S14 and S15 modified with 70 mol% Fe^{2+} and 70 mol% Fe^{3+}, respectively. The Mössbauer spectrum of sample S14 shows one sextet (65.6%) and one doublet (34.4%). The sextet is characterized by the isomer shift (IS) of 0.37 mm s^{-1}, quadrupole shift (QS) of −0.21 mm s^{-1}, line width (LW) of 0.46 mm s^{-1} and hyperfine magnetic field (MF) of 51.0 T. The doublet is characterized by the IS = 0.36 mm s^{-1}, QS = 0.77 mm s^{-1} and LW = 0.44 mm s^{-1}. The Mossbauer spectrum of sample S15 shows a doublet (79.8%) and a sextet (20.2%). The parameters of the doublet are IS = 0.37 mm s^{-1}, QS = 0.76 mm s^{-1} and LW = 0.56 mm s^{-1}, whereas those of the sextet are IS = 0.33 mm s^{-1}, QS = −0.09 mm s^{-1}, LW = 0.42 mm s^{-1} and MF = 51.1 T. The sextet corresponds to α-Fe_2O_3 (hematite) and the doublet to paramagnetic or superparamagnetic particles.

$$Mn^{2+} + Cl_2 + 2H_2O \rightarrow MnO_2 + 2Cl^- + 4H^+ \quad (3)$$

$$4MnO_4^- + 4H^+ \rightarrow 3O_2 + 2H_2O + 4MnO_2 \quad (4)$$

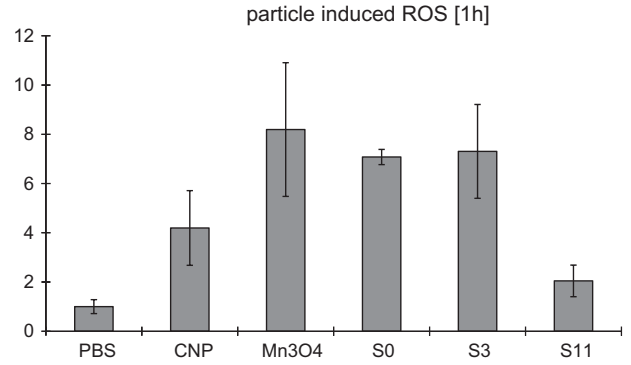

Fig. 10. The flow cytometry determination of intracellular reactive oxygen species (ROS) induced by synthesized manganese oxide nanoparticles. Carbon nanoparticles (CNP) were used as the control. Samples Mn_3O_4 (Fig. 1) S0 and S3 (Fig. 2) revealed much higher amounts of ROS than CNP. Sample S11 (Fig. 5) appeared to induce much lower levels of ROS; however, an increase in fluorescence, which proved to be statistically significant ($p = 0.02$), was also observed.

Upon modification with Mn^{2+} (or Fe^{2+}) the precipitation in the flask started immediately at room temperature prior to autoclaving, because the excess Mn^{2+} (Fe^{2+}) reduced $Mn^{7+}O_4^-$ to $Mn^{4+}O(OH)_2$ [20];

$$2MnO_4^- + 3Mn^{2+} + 7H_2O \rightarrow 5MnO(OH)_2 + 4H^+ \quad (5)$$

The amorphous MnO_2 precipitate, i.e., $MnO(OH)_2$ hydrothermally transformed in the autoclave at 140 °C into various MnO_2 polymorphs, depending on the type of metal cation and synthesis conditions. The addition of Fe^{2+} initiated the precipitation of amorphous manganese and iron oxide. On the other hand, modification with Cu^{2+} and Ni^{2+} started from a clear dark purple solution and precipitation occurred in a hydrothermal condition like in a pure $KMnO_4$ system.

Mn-oxides are interesting when it comes to toxicity studies for two important reasons, (a) they show different structures and morphologies of nanoparticles, and (b) manganese shows a variety of oxidation states, which undergo different oxidation/reduction reactions. Fig. 10 shows the flow cytometry determination of intracellular reactive oxygen species (ROS) induced by synthesized manganese oxide nanoparticles. Carbon nanoparticles (CNPs) were used as a control. Intracellular oxidative stress in epithelial cells is significantly increased by manganese samples after 1 h of incubation ($p < 0.05$). At this juncture, no cytotoxic effects of the samples were observed (data not shown). The chosen doses as a mass equivalent to an accumulative dosage of environmental carbon nanoparticles (CNPs) for samples Mn_3O_4, S0 and S3 revealed much higher amounts of reactive oxygen species (ROS) than CNP. Although S11 appeared to induce much lower levels of ROS, an increase in fluorescence was also observed, which proved to be statistically significant ($p = 0.02$). As we demonstrated earlier, the intracellular induction of ROS is a critical event in cytotoxic and pathogenic events triggered by nanoparticles [21,22]. To further investigate such events, studies on the cellular uptake of the described manganese oxide nanoparticles, and on the source of intracellular ROS will be needed.

Appendix A. Supplementary material

Supplementary data associated with this article can be found, in the online version, at http://dx.doi.org/10.1016/j.molstruc.2012.09.083.

References

[1] F. Rault, E. Pleyber, C. Campagne, M. Rochery, S. Giraud, S. Bourbigot, E. Devaux, Polym. Degrad. Stab. 94 (2009) 955–964.
[2] M.R. Johan, L.M. Ting, Int. J. Electrochem. Sci. 6 (2011) 4737–4748.
[3] R. Frick, B. Müller-Edenborn, A. Schlicker, B. Rothen-Rutishauser, D.O. Raemy, D. Günther, B. Hattendorf, W. Stark, B. Beck-Schimmer, Toxicol. Lett. 205 (2011) 163–172.
[4] C. Wu, W. Xie, M. Zhang, L. Bai, J. Yang, Y. Xie, Chem. Eur. J. 15 (2009) 492–500.
[5] X. Wang, Y. Li, Chem. Eur. J. 9 (2003) 300–306.
[6] X. Huang, D. Lv, H. Yue, A. Attia, Y. Yang, Nanotechnology 19 (2008) 225606 (7pp).
[7] X. Li, W. Li, X. Chen, C. Shi, J. Cryst. Growth 297 (2006) 387–389.
[8] B. Tang, G. Wang, L. Zhuo, J. Ge, Nanotechnology 17 (2006) 947–951.
[9] X. Sun, X. Kong, Y. Wang, C. Ma, F. Cui, H. Li, Mater. Sci. Eng. C 26 (2006) 653–656.
[10] N. Sui, Y. Duan, X. Jiao, D. Chen, J. Phys. Chem. C 113 (2009) 8560–8565.
[11] J. Luo, H.T. Zhu, H.M. Fan, J.K. Liang, H.L. Shi, G.H. Rao, J.B. Li, Z.M. Du, Z.X. Shen, J. Phys. Chem. C 112 (2008) 12594–12598.
[12] M. Gotić, G. Dražić, S. Musić, J. Mol. Struct. 993 (2011) 167–176.
[13] T. Gao, H. Fjellvag, P. Norby, Nanotechnology 20 (2009) 055610 (7 pp).
[14] Q. Feng, K. Yanagisawa, N. Yamasaki, J. Porous Mater. 5 (1998) 153–161.
[15] M. Ristić, S. Musić, S. Popović, Đ. Dragčević, M. Marciuš, M. Ivanda, J. Mol. Struct., submitted for publication.
[16] M. Gotić, S. Ivanković, S. Musić, T. Prebeg, Collect. Czech. Chem. Commun. 74 (2009) 1351–1360.
[17] C.M. Julien, M. Massot, Mater. Sci. Eng. B B97 (2003) 217–230.
[18] Y. Li, J. Wang, Y. Zhang, M.N. Banis, J. Liu, D. Geng, R. Li, X. Sun, J. Colloid Interface Sci. 369 (2012) 123–128.
[19] S. Dash, S. Patel, B.K. Mishra, Tetrahedron 65 (2009) 707–739.
[20] V.N. Alexeyev, Qualitative Analysis, MIR Publisher, Moscow, 1971. p. 281.
[21] A. Weissenberg, U. Sydlik, H. Peuschel, P. Schroeder, M. Schneider, R.P.F. Schins, J. Abel, K. Unfried, Free Radical Biol. Med. 49 (2010) 597–605.
[22] K. Unfried, C. Albrecht, L.O. Klotz, A. von Mikecz, S. Grether-Beck, R.P.F. Schins, Nanotoxicology 1 (2007) 52–71.